Title

Rhesus Macaque Brain Developmental Trajectory: A Longitudinal Analysis Using Tensor-Based Structural Morphometry and Diffusion Tensor Imaging

Journal

Cerebral Cortex, 30(8)

ISSN

1047-3211

Authors

Kim, Jeongchul
Jung, Youngkyoo
Barcus, Richard
et al.

Publication Date

2020-06-30

DOI

10.1093/cercor/bhaa015

Peer reviewed

Cerebral Cortex, August 2020;30: 4325–4335

doi: 10.1093/cercor/bhaa015
Advance Access Publication Date: 2 April 2020
Original Article

ORIGINAL ARTICLE

Rhesus Macaque Brain Developmental Trajectory: A Longitudinal Analysis Using Tensor-Based Structural Morphometry and Diffusion Tensor Imaging

Jeongchul Kim[1,2], Youngkyoo Jung[1,2,3], Richard Barcus[1,2], Jocelyne H. Bachevalier[4,5], Mar M. Sanchez[5,6], Michael A. Nader[7,8,9] and Christopher T. Whitlow[1,2,3,8,9,10]

[1]Radiology Informatics and Image Processing Laboratory (RIIPL), Wake Forest School of Medicine, Winston-Salem, NC 27157, USA, [2]Department of Radiology, Wake Forest School of Medicine, Winston-Salem, NC 27157, USA, [3]Department of Biomedical Engineering, Wake Forest School of Medicine, Winston-Salem, NC 27157, USA, [4]Department of Psychology, Emory University, Atlanta, GA 30322, USA, [5]Division of Developmental and Cognitive Neuroscience, Yerkes National Primate Research Center, Emory University, Atlanta, GA 30329, USA, [6]Department of Psychiatry and Behavioral Sciences, Emory University School of Medicine, Atlanta, GA 30322, USA, [7]Department of Physiology and Pharmacology, Wake Forest School of Medicine, Winston-Salem, NC 27157, USA, [8]Center for Research on Substance Use and Addiction, Wake Forest School of Medicine, Winston-Salem, NC 27157, USA, [9]Clinical and Translational Science Institute, Wake Forest School of Medicine, Winston-Salem, NC 27157, USA, and [10]Department of Biostatistics and Data Science, Wake Forest School of Medicine, Winston-Salem, NC 27157, USA

Address correspondence to Prof. Christopher T. Whitlow, Department of Radiology, Wake Forest School of Medicine, Winston-Salem, NC 27151, USA. Email: cwhitlow@wakehealth.edu

Abstract

The typical developmental trajectory of brain structure among nonhuman primates (NHPs) remains poorly understood. In this study, we characterized the normative trajectory of developmental change among a cohort of rhesus monkeys ($n = 28$), ranging in age from 2 to 22 months, using structural MRI datasets that were longitudinally acquired every 3–4 months. We hypothesized that NHP-specific transient intracranial volume decreases reported during late infancy would be part of the typical developmental process, which is driven by volumetric contraction of gray matter in primary functional areas. To this end, we performed multiscale analyses from the whole brain to voxel level, characterizing regional heterogeneity, hemispheric asymmetry, and sexual dimorphism in developmental patterns. The longitudinal trajectory of brain development was explained by three different regional volumetric growth patterns (exponentially decreasing, undulating, and linearly increasing), which resulted in developmental brain volume curves with transient brain volumetric decreases. White matter (WM) fractional anisotropy increased with age, corresponding to WM volume increases, while mean diffusivity (MD) showed biphasic patterns. The longitudinal trajectory of brain development in young rhesus monkeys

follows typical maturation patterns seen in humans, but regional volumetric and MD changes are more dynamic in rhesus monkeys compared with humans, with marked decreases followed by "rebound-like" increases.

Key words: diffusion tensor imaging, magnetic resonance imaging, neurodevelopment, primates, rhesus macaque, tensor-based morphometry

Introduction

Mapping the nonhuman primate (NHP) brain with longitudinally acquired structural magnetic resonance imaging (MRI) can provide valuable translational scientific insights into pathological changes in human brain development. Rhesus macaques have a lifespan of about 25 years, and their developmental stages are 3–4 times faster than humans (Scott et al. 2016). Because rhesus macaques have neuroanatomy, social skills, and psychological characteristics similar to humans, they have been widely used in MRI studies to infer normal human brain development (Malkova et al. 2006; Payne et al. 2010; Shi et al. 2013; Scott et al. 2016; Meng et al. 2017), as well as developmental disorders (Braunschweig and Van de Water 2012; Bauman et al. 2013). In particular, NHP models are useful to investigate the effects of drug exposure and maternal environments on brain structural changes associated with development. For example, chronic alcohol drinking among NHPs at younger ages is related to greater magnitude gray matter (GM) volumetric decreases as adults (Kroenke et al. 2014). Maternal influenza infection during gestation (considered a prenatal risk of schizophrenia) was associated with abnormally smaller cortical GM volume and white matter (WM) volumes in cingulate and parietal areas at approximately 1 year of age (Short et al. 2010). The intake of a dissociative drug (phencyclidine) during late infancy in rhesus monkeys was associated with increased WM maturation and volume compared with normal controls (Liu et al. 2015). Additionally, the effects of immunoglobulin G–class antibody in an autism spectrum disorder model were evaluated by longitudinal MRI, demonstrating WM enlargement in frontal lobes for 2 years after birth (Bauman et al. 2013). To reliably interpret structural brain tissue volumetric changes measured via longitudinally acquired MRI, and to decide whether these structural changes are drug-/disease-specific, a detailed understanding of the typical brain developmental trajectory of rhesus macaques based on longitudinal MRI is necessary, with a shorter interscan interval and longer study period.

Prior longitudinal MRI studies of rhesus monkey brain development have demonstrated relatively rapid volumetric increases over the first several months after birth, followed by stabilized growth patterns after infancy characterized by quadratic (Knickmeyer et al. 2010) or cubic (Payne et al. 2010; Liu et al. 2015) curves. However, other recent longitudinal studies in NHPs (Malkova et al. 2006; Scott et al. 2016) have reported that intracranial volume (ICV) decreases slightly during late infancy (months 6–10), driven primarily by volumetric contractions of the occipital and parietal lobes, followed by an apparent rebound in ICV up to 3 years of age. These changes were interpreted by the investigators as possible growth or plateau periods based on interactions between earlier GM maturation and continued WM growth. However, it is critical to elucidate the mechanisms of these somewhat unexpected NHP brain volumetric decreases in late infancy to avoid misinterpretation of imaging biomarkers derived from NHP studies.

Although previous studies have provided valuable insights into dynamic brain growth patterns among NHPs, these dynamic volumetric changes were described only in the whole brain or within large regions of interest (ROIs). Less is known, however, about potential local structural mechanisms that may be driving these intracranial developmental volumetric changes in rhesus monkeys. For example, how WM microstructure changes during this period of relatively rapid brain development remains unclear due to the lack of diffusion tensor imaging (DTI) data. Although recent investigations have studied brain developmental trajectory using longitudinal MRI and DTI (Liu et al. 2015; Meng et al. 2017), the small number of normal NHPs and relatively sparse scan intervals limited the characterization of brain developmental trajectory.

To distinguish abnormal from normal brain development, patterns of brain growth can be measured at different observation scales based on longitudinal multimodal MRI data. Thus, in this study, we characterize the normative trajectory of developmental change in a publicly available dataset of rhesus monkeys from late infancy to juvenile stages (months 2–22), using longitudinal structural MRI and DTI repetitively acquired every 3–4 months. We hypothesized that NHP-specific transient ICV decreases reported during late infancy would be part of the typical developmental process, which is driven by volumetric contraction of GM in primary functional areas. We analyzed longitudinal volumetric changes of different brain regions and their effects on overall global volumetric change, using a multiscale analysis from the whole brain to voxel-wise level. In addition, we analyzed the relationships between WM volumetric change and DTI metrics, including fractional anisotropy (FA) and mean diffusivity (MD).

Materials and Methods

MRI Dataset

Longitudinal brain MRI datasets (T_1-weighted [T_1w], T_2-weighted [T_2w], and diffusion-weighted images) acquired from a cohort of normally developing rhesus monkeys were downloaded from a publicly available database (UNC-Wisconsin Neurodevelopmental Rhesus Data at https://data.kitware.com). All infants were born between June 2011 and August 2013 and reared naturally by their mothers until weaning, which occurred at 6–7 months of age. Eight monkeys from the total of 36 were included in the cohort within 30 days after birth (also scanned between 2 and 22 months of age). Afterward, the older juveniles were housed in small social groups or as a pair to provide companionship. This rearing and housing strategy was designed to facilitate their normal socialization and to ensure standardized rearing conditions. This longitudinal primate database was created by the Harlow Primate Lab at the University of Wisconsin-Madison and the Neuro Image Research and Analysis Laboratories (NIRAL) at UNC-Chapel Hill (Styner et al. 2007; Young et al. 2017). All NHPs were members of a large 500+ monkey-breeding colony, with known history extending back 5 generations and over 25 years.

All NHPs were scanned longitudinally every 3–4 months on a GE Signa 3-T scanner (General Electric Medical Systems) in

the Waisman Center at University of Wisconsin-Madison. T_1w images were acquired using a high-resolution axial 3D IR-SPGR sequence (time repetition [TR] = 8.6 ms, time echo [TE] = 2.0 ms, field of view [FOV] = 14 cm, flip angle = 10°, matrix = 512 × 512, voxel size = 0.27 mm, slice thickness = 1 mm, slice gap = 0.5 mm, bandwidth = 15.63 kHz) with an effective voxel resolution of $0.27 \times 0.27 \times 1.5$ mm^3. A spin-echo sequence was used to acquire T_2w images (TR = 12 000 ms, TE = 90 ms, FOV = 14 cm, flip angle = 90°, matrix = 512 × 512, voxel size = 0.27 mm, slice thickness = 1.5 mm, slice gap = 0 mm, bandwidth = 31.25 kHz). Diffusion-weighted images (DWIs) were acquired using an echo-planar imaging (EPI) sequence ($0.55 \times 0.55 \times 2.5$ mm^3) with 120 diffusion encoding directions at $b = 1000$ s/mm^2 and a single base image at $b = 0$. The in-plane resolution was upsampled in k-space by a factor of 2 on the scanner.

Ketamine hydrochloride (10 mg/kg intramuscular [IM]), followed by medetomidine (50 µg/kg IM) was used for immobilization during scanning. All monkeys were oriented identically within a stereotaxic platform; situated within the human eight-channel brain array coil. Similar head positions were verified in the sagittal and coronal planes on the scanner.

Image Registration and Processing

T_1w, T_2w, and manually defined brain mask images are available from the publicly available database. These images were rigidly aligned to the UNC Primate Atlas (https://www.nitrc.org/projects/primate_atlas) that was built from the T_1w and T_2w images using a developmental training dataset of 18 cases aged 16–34 months, with labels that include 26 cortical and 10 subcortical regions (Styner et al. 2007). Quality-controlled (QCed) DWIs and processed diffusion scalar (FA and MD) images in the native subject space are also available. Using these T_1w, T_2w, and QCed DWI images, we analyzed longitudinal volumetric changes at different scales (from the whole brain to voxel level) and corresponding regional diffusion properties of WM across the multiple time points. For longitudinal analysis, 28 NHPs (12 females and 16 males) between 2 and 22 months of age were selected (Fig. 1). We excluded 8 NHPs from the total of 36 because they were not available from the database or did not have enough imaging time points (minimum 3) for longitudinal MRI analysis.

Individual T_1w image preprocessing steps included denoising (Tristan-Vega et al. 2012) to reduce background noise and improve tissue contrast for manual tissue segmentation. We performed skull stripping using manually defined brain masks available from the downloaded dataset. After rigid alignment to the NHPs' final time point, within-subject registration of T_1w images across the data acquisition time points was performed using Advanced Normalization Tools (ANTs) (Penn Image Computing and Science Laboratory, University of Pennsylvania) and nonlinear registration algorithm (Avants and Gee 2004). Based on the deformation field between a pair of images within the subject, the voxel-wise volume change ratio (Jacobian determinant [JD]) was calculated using an in-house tensor-based morphometry algorithm (Kim et al. 2016). JD represents the slope of volume–age curves at the voxel level between two time points, which provides information on the phase of growth (volumetrically expanding or contracting) during the measurement time period. The 1-mm size of the Gaussian smoothing kernel was applied to the combined deformation fields (affine + deformable) to improve statistical power and reduce registration mismatch. For voxel-wise statistical analyses, as shown in Figure 2, individual

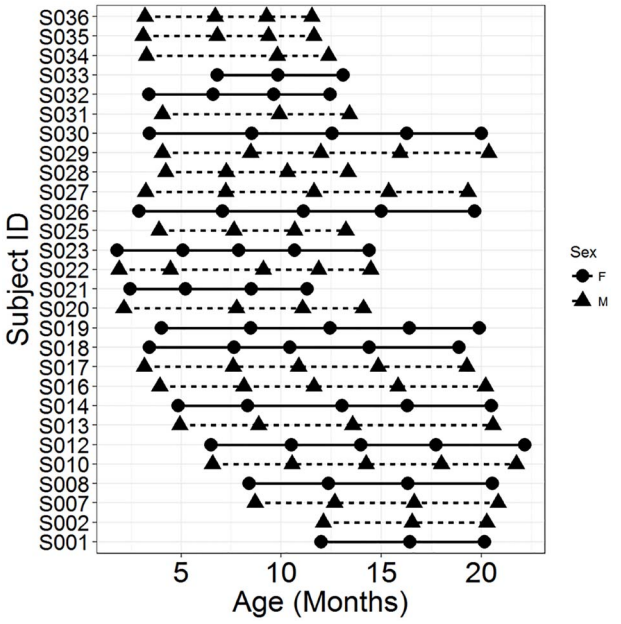

Figure 1. Age at the time of scans for 12 female rhesus monkeys and 16 male rhesus monkeys. Each of 119 scans obtained is represented by a circle (female) or triangle (male). Each of the 28 monkeys is shown in a different row, with their scans connected by a solid line (female) or dotted line (male).

volumetric change (JD) maps for each period were registered to the study-specific template (SST) by applying two nonlinear transforms (individual JD map on the previous time points → subject's final time point → SST). Here, an unbiased SST was created from the final time point T_1w images of 28 NHPs using ANTs.

We performed an automatic brain segmentation of SST into GM, WM, and cerebrospinal fluid (CSF) using probabilistic tissue maps from pre-existing pediatric-specific UNC Primate Brain Atlas as priors. The Gibbs ringing artifacts (typically appearing as multiple fine parallel lines immediately adjacent to high-contrast interfaces) (Czervionke et al. 1988) observed on the generated template (SST) around the boundaries of gray matter and CSF caused misclassification of GM as WM. These artifacts were manually reclassified correctly by two experienced imaging experts (JK and RB). To ensure the manual correction, we estimated the target overlap ratio (TO_r) between two imaging experts; TO_r was defined by the intersection between two similarly labeled regions in source S and target T divided by the volume of the regions in T (Klein et al. 2009). A high interrater reliability in the artifact correction was observed showing TO_r values of 0.97 for CSF and 0.99 for GM. New probabilistic tissue maps of the SST were generated by smoothing images of posterior probability maps (Tustison et al. 2017).

At the individual NHP level, an automatic tissue segmentation was performed using T_1w and T_2w images because multimodal anatomical images may provide more robust outcomes in tissue segmentation, particularly in neonatal brain tissue classification (Prastawa et al. 2005; Weisenfeld and Warfield 2009). The joint T_1w- and T_2w-based tissue segmentation of ANTs uses an iterative algorithm between bias-field corrected segmentation maps (Avants et al. 2011). Here, to help initial segmentation, tissue priors of each time point were derived from the tissue probability maps of SST by applying nonlinear (between SST and the final time point image) and affine

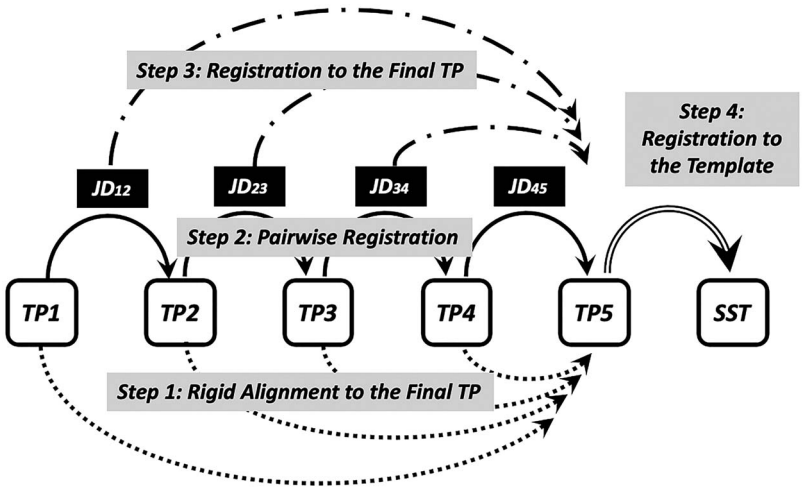

Figure 2. Longitudinal registration steps from within-subject to the study-specific template (SST). After rigid alignment to the final time point image within the subject (Step 1), the period-specific volume changes (JD) were estimated from the pair-wise registration (Step 2), which were registered to the final time point (Step 3). Finally, the images on the final time point were registered to the SST (Step 4).

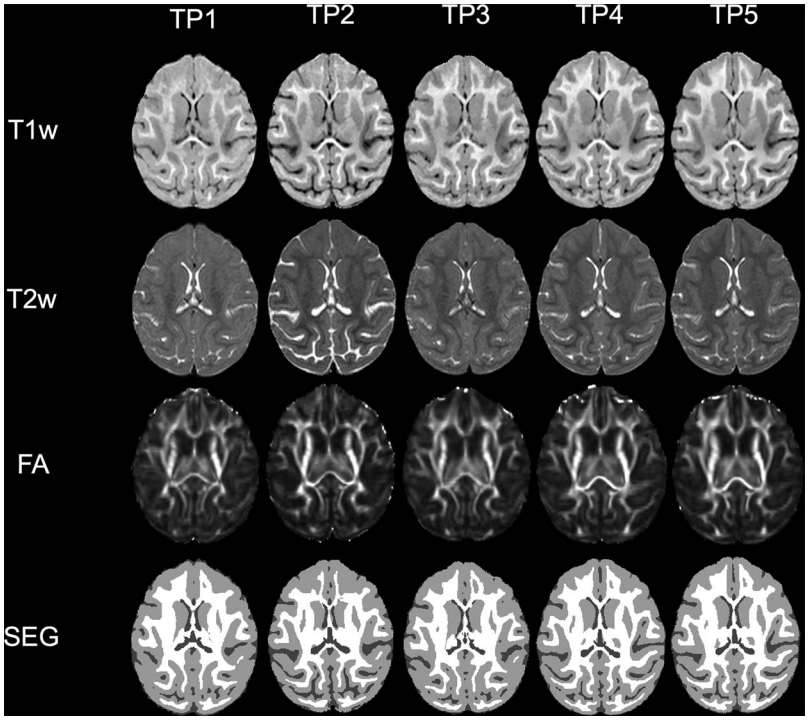

Figure 3. An example longitudinal T_1w, T_2w, FA, tissue segmentation map (SEG) images for a single rhesus monkey at months 3 (TP1), 7 (TP2), 11 (TP3), 15 (TP4), and 19 (TP5).

(between the final time point image and the previous time point images within the subject) transforms. Finally, to correct segmentation errors around the internal and external capsules due to low tissue contrast in T_1w and T_2w images, we applied the age-adaptive FA threshold to separate WM from GM (Fig. 3). To find an age-adaptive FA threshold for each individual at multiple time points, all individual FA images were warped to the SST and mean FA values at WM–GM boundary were extracted.

The parcellation map defined in the UNC Primate Brain Atlas was warped to the SST using deformable registration and manually corrected. The full parcellation consists of separate definitions for the left and right hemispheres for the subcortical, frontal, prefrontal, cingulate, parietal, occipital, auditory, visual, and limbic temporal lobes, as well as the brainstem, corpus callosum, and cerebellum. Cortical labels in the parcellation map include GM, WM, and CSF and subcortical structures, including the hippocampus, amygdala, caudate, and putamen. The corrected parcellation map of SST was then warped to each NHP's time point using the same transforms applied in the individual tissue segmentation process above.

The QC was performed with DTIPrep (Liu et al. 2010; Oguz et al. 2014), and QCed DWIs, FA images, and MD images are

available from the database. This tool allows for image viewing, image cropping, checking *b*-values, checking gradient vectors, noise filtering, evaluating correlation intensities to check for brightness and venetian blind artifacts, as well as detection of vibration artifacts, and artifact correction (motion and eddy current). We re-estimated DTI scalars from the QCed DWIs to confirm the results using an FMRIB Software Library function, *dtifit* (Wellcome Centre for Integrative Neuroimaging, University of Oxford). Next, the brain mask of a representative NHP was manually created in B0 image space, and the brain mask was nonlinearly registered to the other NHP's B0 images with ANTs (*antsRegistrationSyNQuick.sh*). With regard to coregistration of each NHP's T_1w image and B0 image, because the affine registration was not able to properly match the anatomical boundaries between the T_1w image and B0 image, nonlinear transforms between the FA image (available from the pre-existing dataset) and corresponding T_1w image were applied. Parcellation maps on T_1w images were also warped to the DWI space for ROI analysis using the nonlinear transforms from T_1w to FA images.

We reviewed the accuracy of nonlinear registration, tissue segmentation, and coregistration by two experienced imaging experts (JK and RB) and a neuroradiologist (CTW). Based on the manual segmentation of hippocampal regions, TO_r was estimated for all scans (see Table S1) to check the accuracy of nonlinear registration. The quality of automatic tissue segmentation was assessed using randomly selected 28 images and demonstrated TO_r values for GM (0.95 ± 0.02) and WM (0.87 ± 0.05). The coregistration between FA and T_1w images was visually inspected by experienced imaging experts (JK and RB).

Statistical Analysis

We used a multiscale analysis approach to analyze the developmental patterns from the whole brain to the voxel level, with the aim of confirming regionally heterogeneous volumetric changes and to obtain additional insights into local volume changes within the defined ROIs. For longitudinal regression analysis at the whole brain and ROI levels, we used the generalized additive mixed model function (*gamm4*) in the R statistical package (version 3.3.3: http://r-project.org) to fit complex growth patterns with smoothing splines to determine age differences, sex differences, and left-to-right asymmetry of brain growth patterns. ICVs were measured directly from the manually defined brain masks, and ROI volumes were measured using the parcellation map warped to the individual brain. The trajectory of ICV divided by body weight was also estimated to determine the ratio of brain to body size during development. Diffusion properties (FA and MD) in whole WM and ROIs were also fitted using the same *gamm4* function. Bonferroni correction was applied for multiple comparisons in ROI analyses: The adjusted *P* value was estimated from the desired alpha level (0.05) divided by the number of cortical and subcortical regions (26 ROIs) used in the analyses.

For voxel-wise statistical analyses, individual volumetric change (JD) maps for each period were registered to the SST. Due to difficulty in interpretation of statistical estimates for more than 800 000 voxels, we employed relatively simple linear mixed-effect model instead of *gamm4*. The *lme* function of MATLAB R2014b (MathWorks) was applied to confirm the trajectory of the volumetric change ratio, with age and sex as covariates. The false discovery rate (Benjamini and Hochberg 1995) was applied to correct for multiple comparisons. Adjusted *P* values less than 0.05 were considered statistically significant.

Results

Volumetric Change

We describe our volumetric analysis results based on three different scales: whole brain, ROI, and voxel levels. Longitudinal plots of ICV showed undulating patterns of developmental change from months 2 to 22 (Fig. 4*b*), as follows: ICV increased with GM, WM, and CSF from 2 to 5 months. GM and CSF volumes decreased while WM volume continued to increase from months 5 to 9, which resulted in an overall net ICV decrease. ICV appeared to rebound, with simultaneous GM and WM volume increases after 9 months until 22 months, whereas CSF volume remained stable during this period. Left hemisphere–dominant growth was observed, as characterized by volumetric increases for WM and CSF ($P < 0.001$), with no differences between males and females. Details of model estimates of volumetric growth trajectory for GM, WM, and CSF are summarized in Supplementary Tables S2 and S3. To better explain the different volumetric growth rates of brain tissues, the derivatives (slope) of volume curves are represented in Figure 4*c*. Positive values of the curve indicate volumetric increases/expansion, whereas negative values indicate volumetric decreases/contraction. The reflection points of tissue volume curves (blue arrows in Fig. 4*b*) correspond to the *x*-intercepts in the curves of the derivatives, which indicate the period of volumetric contraction during brain development in rhesus monkeys. ICV, GM, and CSF demonstrated different timing of volumetric contraction from 4.5, 4.2, and 6.3 months to 8.8, 8.0, and 11.5 months, respectively (Fig. 4*c*). During this period, ICV change was dominated by GM volume change. As observed in Figure 4*b*, no volumetric contraction was observed in WM during the study period. Even though ICV patterns fluctuated during the study period, ICV-to-body weight (IVC–BW) ratios demonstrated a relatively consistent pattern characterized by exponential decreases, which approach levels seen in adults at the later time points (Fig. 4*d*). Specifically, there were relatively rapid decreases in IVC–BW ratios until 9 months of age, followed by a slower rate of decrease thereafter (Fig. 4*d*). No hemispheric difference or sex difference was observed in the ICV–BW ratio.

Changes in the whole brain and segmented tissue volumes were assigned into 26 cortical regions defined by UNC Primate Brain Atlas labels in order to identify regional heterogeneity in growth. Regional growth trajectories were classified into three groups: 1) exponentially decreasing ROIs, 2) undulating ROIs as observed in the whole brain (i.e., volumetric decreases between 5 and 9 months, followed by rebound-like volumetric increases thereafter), and 3) linearly increasing ROIs (i.e., continuous volumetric increases with age, without marked transient volumetric decreases). Corresponding ROIs for different growth patterns are listed in Table 1. Considering these three different regional patterns of volumetric change, as well as undulating ICV change with age (Fig. 4*b*), the undulating ROIs were linearly correlated with the whole brain volume, while linearly increasing ROIs demonstrated independent growth patterns. For example, ICV demonstrated a linear relationship with frontal lobe volume (FLV) in our analyses ($ICV = 6.54 \times FLV + 21\,743$, $R2 = 0.86$, $P < 0.001$), while subcortical volume did not.

Figure 5 shows volumetric changes in representative (the largest) ROIs reflecting three different patterns described in

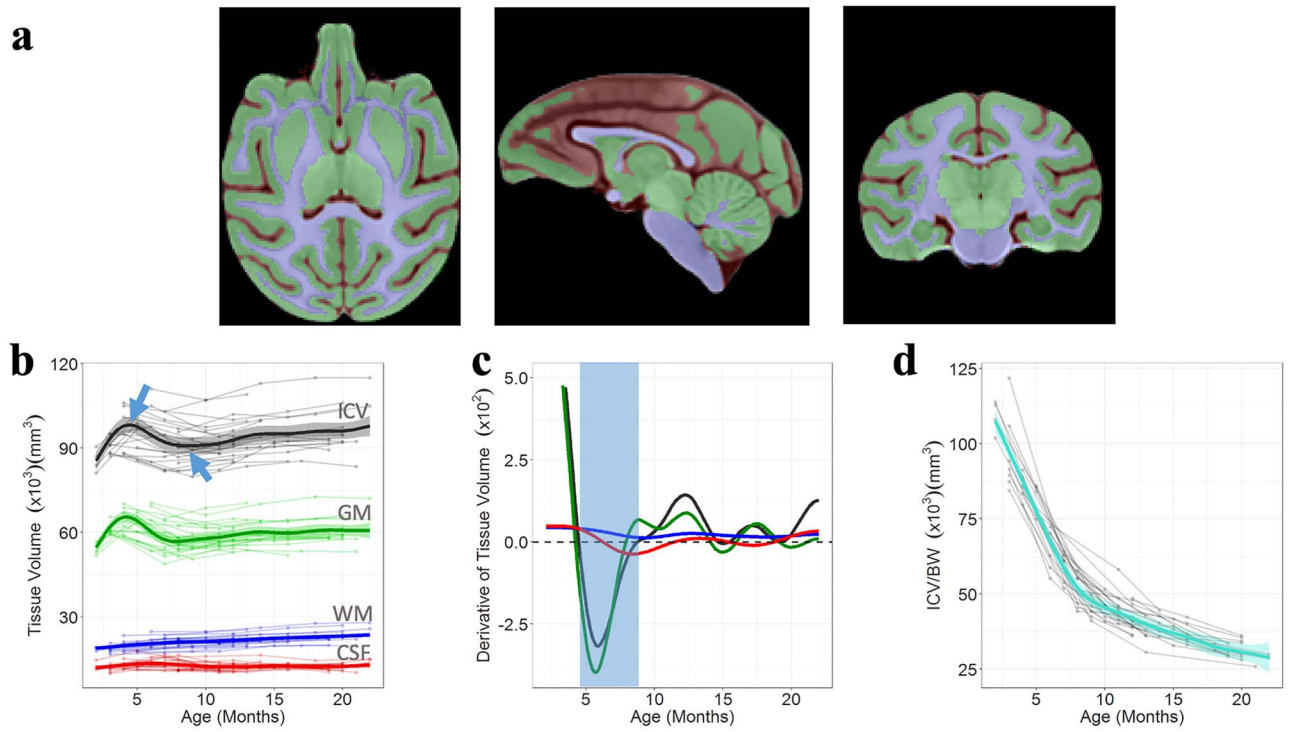

Figure 4. (*a*) Tissue segmentation map of study population-specific template (PST). (*b*) Longitudinal trajectories of intracranial, gray matter, white matter, and cerebrospinal fluid volumes. Blue arrows indicate the positive peak and the negative peak of intracranial volume (ICV), which corresponds to the volume decrease/contraction period. Circles connected by solid lines represent individual trajectories; thick solid lines show predicted responses in the 28 rhesus monkeys. (*c*) Derivatives of tissue volume–age curves demonstrate that the shift in the growth phase is driven by GM during the period of ICV contraction. (*d*) However, ICV-to-body weight (BW) ratio continues to decrease with age.

Table 1 Volumetric growth, FA and MD patterns in brain regions of rhesus monkeys from 2 to 22 months after birth

ROI	Tissue volume	FA (WM only)	MD (WM only)
Occipital	Exponentially decreasing	Logarithmically increasing	Rebounding
Parietal	Exponentially decreasing	Logarithmically increasing	Rebounding
Temporal visual	Exponentially decreasing	Logarithmically increasing	Rebounding
Temporal auditory	Undulating	Logarithmically increasing	Rebounding
Frontal	Undulating	Logarithmically increasing	Exponentially decreasing
Cingulate	Undulating	Logarithmically increasing	Exponentially decreasing
Prefrontal	Undulating	Logarithmically increasing	Exponentially decreasing
Subcortical	Linearly increasing	Logarithmically increasing	Rebounding
Cerebellum	Linearly increasing	Logarithmically increasing	Rebounding
Insula	Linearly increasing	Logarithmically increasing	Rebounding
Corpus callosum	Linearly increasing	Linearly increasing	Exponentially decreasing
Temporal limbic	Linearly increasing	Linearly increasing	Rebounding
Pons and medulla	Linearly increasing	Logarithmically increasing	Rebounding

Table 1. Marked volumetric contraction was observed in occipital, parietal, and temporal visual regions (Fig. 5*b*) from 4 to 10 months, followed by a period of stabilization. Volumetric contraction during this period was dominated by decreased GM volume. We observed undulating patterns of volumetric change in frontal, prefrontal, temporal auditory, and cingulate cortex, as were also observed with whole brain measures. Although these patterns were dominated by GM increases, continued WM volumetric increases led to apparent rebounds in total ROI volumes after 9 months (Fig. 5*c*). Males had higher GM ($P = 0.0291$) and WM ($P = 0.031$) volumes in prefrontal regions compared with females. Subcortical, cerebellum, insula, and temporal limbic regions showed patterns of relatively rapid increase (Fig. 5*d*). The pons, medulla, and corpus callosum also showed linear increases dominated by WM. Left-sided asymmetry was also observed in most regions in terms of total tissue volume, while temporal auditory and pons and medulla demonstrated right-sided asymmetry. Figures and details of model estimates of volumetric growth trajectory for all ROIs are summarized in Supplementary Figure S2 and Tables S2 and S3.

To confirm regionally heterogeneous volumetric growth patterns and obtain additional insight into local volume changes within the defined ROIs, we derived mean voxel-wise volume change ratio (JD) maps for five periods (3–6, 6–9, 9–12, 12–16, and

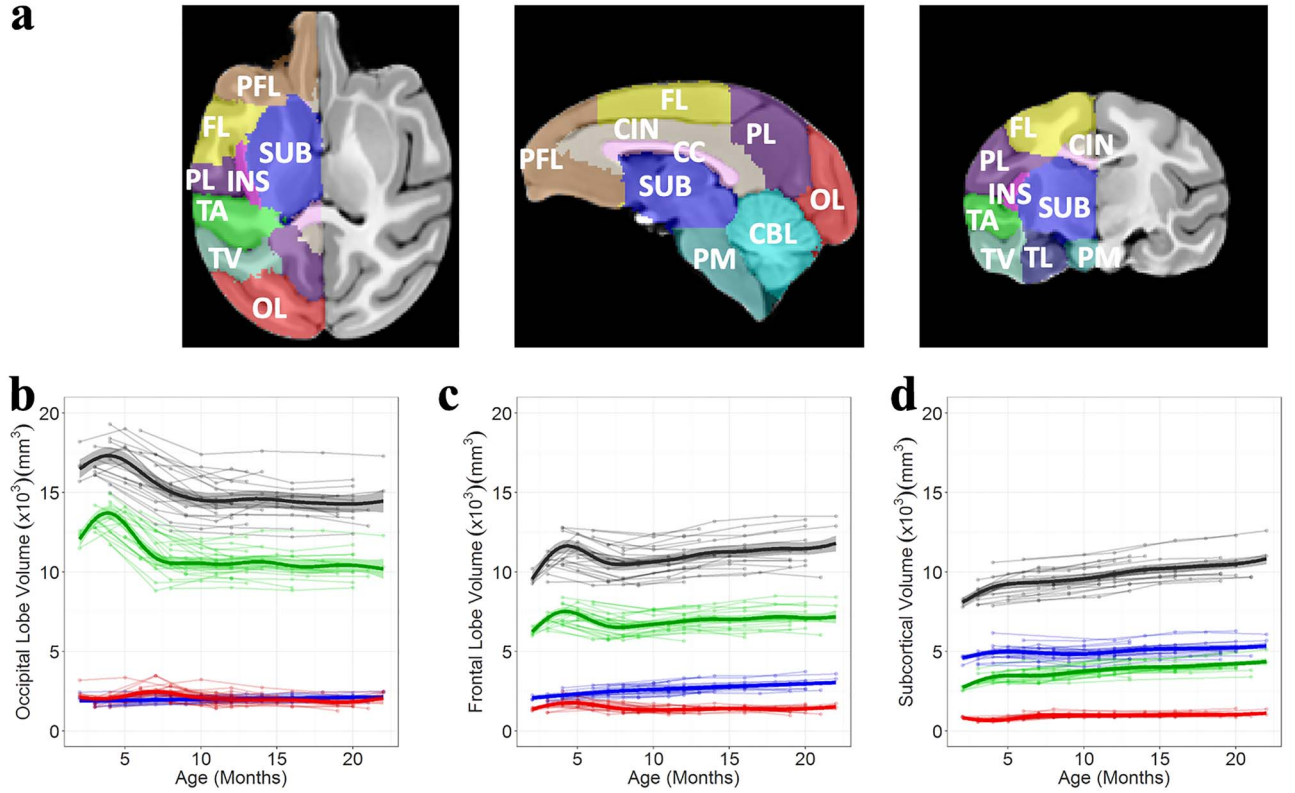

Figure 5. (*a*) Cortical and subcortical regions defined in SST according to UNC Primate Atlas label: Subcortical (SUB), frontal (FL), prefrontal (PFL), cingulate (CIN), parietal (PL), occipital (OL), temporal auditory (TA), temporal visual (TV), temporal limbic (TL) lobes, corpus callosum (CC), and cerebellum (CBL). (*b–d*) Longitudinal changes in tissue volumes in occipital lobes, frontal, and subcortical regions. Different volume change patterns (exponentially decreasing, undulating, linearly increasing) with age are shown, as reported in Table 1. Circles connected by solid lines represent individual trajectories; thick solid lines show predicted responses in the 28 rhesus monkeys.

16–20 months) (Fig. 6). JD does not represent local volume at a single time point, but rather, the local volume change "ratio" between two time points, which can be correlated with the slope of volume–age curves of the whole brain or ROIs. JD > 1.0 means volumetric expansion, while JD < 1.0 implies volumetric contraction compared with baseline of each period. Active volume changes (higher or lower JD values) were observed from 3 to 9 months. Growth patterns became stable thereafter, showing JD values around 1.0 in most regions of the brain (9–20 months). Mean JD maps also consistently correlated with whole brain and ROI volume changes from 3 to 6 months and from 6 to 9 months, with local volumetric contraction (blue-colored areas) in occipital, parietal, and temporal regions and active volumetric expansion (red-colored areas) in the subcortical and frontal regions. Using a linear mixed-effect model, significant age effects on JD were found in some areas of the parietal, occipital, and temporal lobes (green-colored area in the first row of Fig. 6). These clusters showed positive slopes in the JD–age curves representing volumetric contraction during the earlier periods, followed by volumetric expansion in the later periods. This pattern at the voxel level was like that observed with whole brain growth patterns (Fig. 4) and most ROIs (Figs 5 and S2).

DTI Metric Change in WM

We describe our DTI results (FA and MD) in WM at whole brain and ROI levels. Whole brain FA demonstrated patterns approximating logarithmic increases with age (Fig. 7). A relatively rapid increase in FA was observed until 8 months after birth, followed by a smaller increase between 8 and 20 months. Alternatively, whole brain MD showed a biphasic pattern, with high intra-/intersubject variability. In general, MD decreased until 8 months, with an apparent rebound in MD thereafter. Combined FA and MD results demonstrated increasing FA and decreasing MD until 8 months of age, with simultaneously increasing FA and MD after 8 months. No sex differences were observed in the patterns of change in FA and MD, but a lower MD value was observed in the right hemisphere ($P < 0.001$).

There was also regional heterogeneity of age-related change in FA and MD. Regional FA changes were classified as logarithmic or linear, while MD changes were explained by a pattern of exponential decreases or rebound (Fig. 7). Corresponding ROIs are listed in Table 1. Left-sided asymmetry in FA was observed within the insula, temporal visual, pons, and medulla regions, while right-sided asymmetry was observed within subcortical and prefrontal areas (Fig. S3). Alternatively, right-sided asymmetry was observed in MD across most brain regions (Fig. S4). Model estimates including details of hemispheric asymmetry and male versus female asymmetry are summarized in Table S3.

Discussion

In this study, we have quantitatively characterized the trajectory of developmental changes among a cohort of rhesus monkeys using longitudinal structural MRI and DTI from late infancy to juvenile periods (months 2–22). Multiscale analyses from

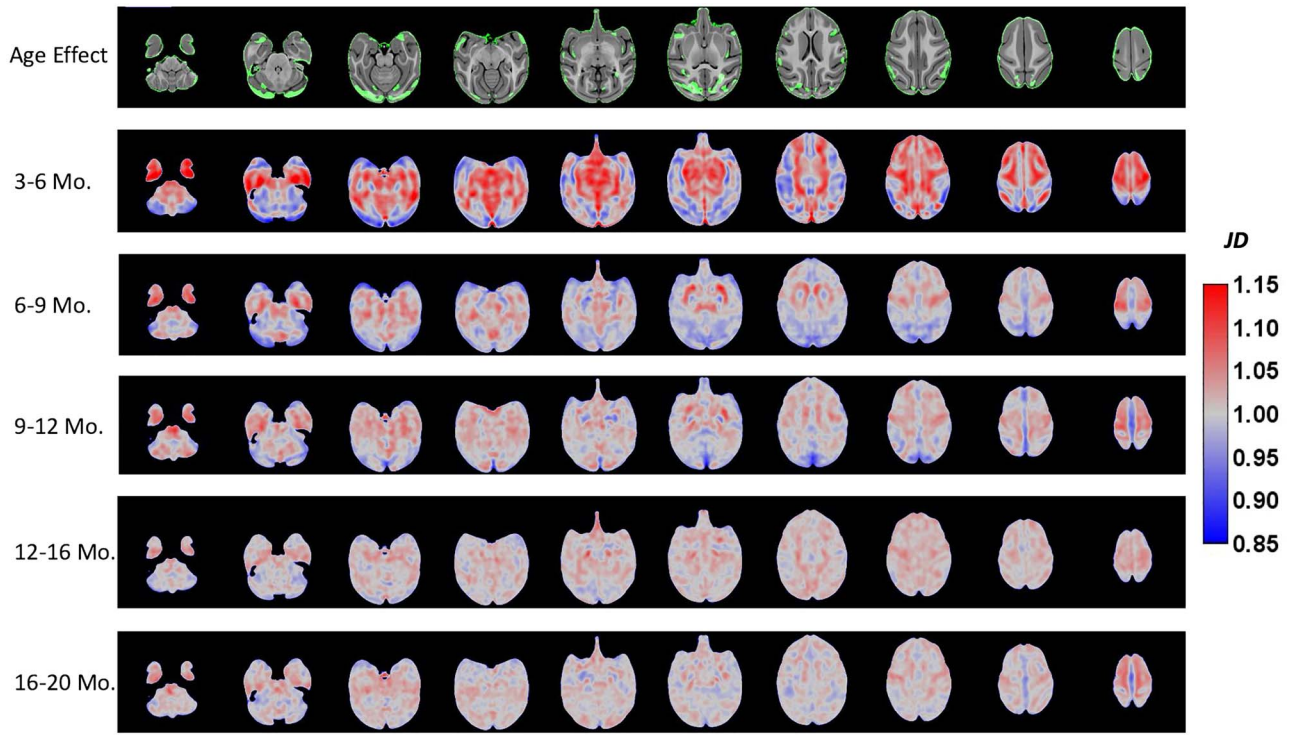

Figure 6. Map of significant results from linear mixed-effect model analyses (first row) and mean volume change rate (JD) maps for each period (second row to the last row). Green-colored areas in the first row demonstrate a significant age effect on volume change rate during the study period, which corresponds to JD value changes from blue (3–9 months) to red (9–20 months) with age. JD = 1.0 means no volumetric change at the voxel level; JD > 1.0 means volumetric expansion, while JD < 1.0 means volumetric contraction during the period.

the whole brain to the voxel-level provided evidence of various patterns of brain growth during development. As reported previously (Malkova et al. 2006; Scott et al. 2016), our results also demonstrated transient decreases in ICV between 5 and 9 months. This volumetric contraction was prominent in occipital, parietal, and temporal lobes during this period. From the individual volumetric measurements, we have confirmed that ICV decreases for our study cohort during this developmental period and that the ICV decreases were driven by GM volume decreases.

Explanations for the transient decrease in ICV reported in previous studies have proposed weaning of infants as a potential etiology, with restricted access to nursing, along with increased physical activity and nutritional status changes (Vandeleest and Capitanio 2012), which may explain specific transient decreases we also observed in ICV around the weaning period (6 months of age). Other studies have reported transient decreases in ICV between 5 and 9 months of age regardless of the timing of weaning (after birth vs. 6–7 months), housing conditions (individually housed vs. grouped with peers), size of the housing (half-acre enclosures vs. 0.25–0.73 m^3), and age of the first MRI scan (Malkova et al. 2006; Scott et al. 2016).

The transient ICV and GM decreases we observed were associated with simultaneous WM volume and FA increases. As such, behavioral or nutritional status changes from breast milk to solid foods may lead to metabolic signals altering whole brain volume with primary effects on GM. An alternative explanation is that progressive neurodevelopmental processes, such as axonal outgrowth and dendritic maturation, are transiently outpaced by regressive processes, such as axonal retraction and programmed cell death/pruning (LaMantia and Rakic 1990). Based on our observation, the structural mechanism for transient decreases in ICV dominating the brain developmental trajectory between 5 and 9 months after birth can be explained by "local GM volumetric contractions" within occipital, parietal, temporal visual, temporal auditory, cingulate, and insula regions (Figs 5 and S2). These regions correspond to volumetrically contracted areas (blue-colored regions in JD maps) during this period (Fig. 6), which further supports that regressive processes between 5 and 9 months are characteristic in rhesus monkey brain development. In addition, the typical decrease in GM volume during this period can be explained by the outward shift of GM during brain development with increase in GM density: over time, myelination could increase the intensity of T_1w images at GM–WM junctions, with the resultant tissue segmentation resulting in decreased GM fractions (Gennatas et al. 2017).

From ROI and voxel-wise volumetric analysis results, dynamic patterns of GM maturation were observed in caudorostral and dorsoventral directions (Figs 5 and S2), as is typical in human brain development (Gilmore et al. 2012; Olson et al. 2012). In addition, GM maturation in humans is much slower than in rhesus monkeys. Based on our fitted data, it took only 2.2 months (from 4.2 to 6.4 months) to reach 10% volumetric contraction of GM (Fig. 4), but 8–9 years for those changes to occur in a longitudinal study of human brain development across adolescence (Tamnes et al. 2017). This marked difference in GM maturation rate could be related to the influence of a longer postnatal experience on brain structure in humans compared with NHPs. The rebounding patterns of ICV among rhesus monkeys around 9 months after birth reflected a shift from GM-driven growth to WM-driven growth during late

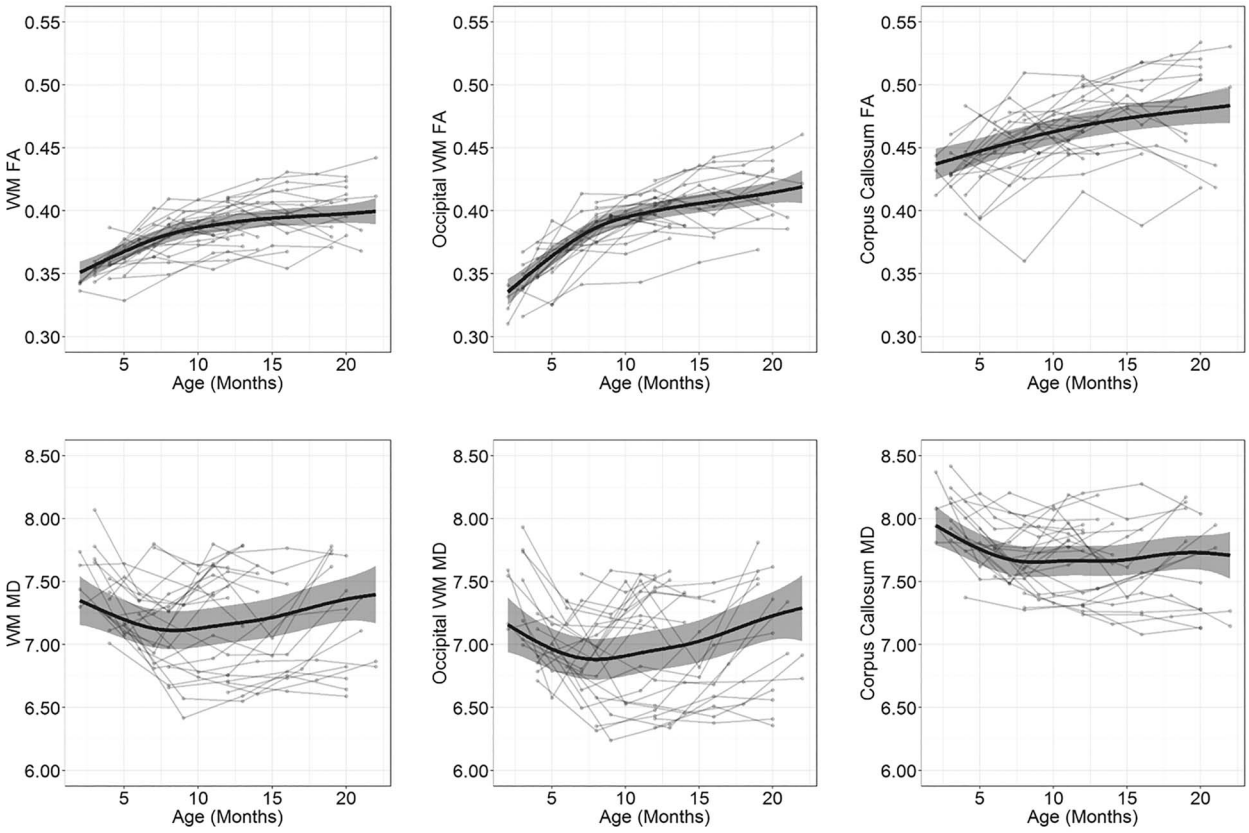

Figure 7. Fractional anisotropy (upper) and mean diffusivity (lower) changes with age for whole brain white matter (left), occipital lobes (middle), and corpus callosum (right). Circles connected by solid lines represent individual trajectories; thick solid lines show predicted responses in the 28 rhesus monkeys.

infancy. These findings are also comparable to human brain development. A systematic review of human brain volume change throughout life (Hedman et al. 2012) reported that ICV reaches its peak at around 10.5 years of age in girls and at around 14.5 years of age in boys. Another study (Lenroot et al. 2007) reported that GM volume starts to decrease around 8.5 years of age in girls and 10.5 years of age in boys and the decline is greater in girls during adolescence. The slight rebound in human brain volume from 20 to 30 years of age suggests a possible second growth of ICV in early adulthood (Hedman et al. 2012) dominated by WM volume increases that continue up to 50 years of age (Westlye et al. 2010).

Previous MRI studies have reported that FA increases and MD decreases with age in both humans and NHPs (Lebel and Beaulieu 2011; Shi et al. 2013; Liu et al. 2015). This parallels our results from birth until 8 months of age. However, between 8 and 22 months after birth, we observed simultaneous increases in FA and MD (Fig. 7). Similar results have been reported previously in temporal auditory, temporal limbic, occipital, pons, and medulla regions between 300 and 900 days after birth in a cross-sectional study of rhesus monkey (Shi et al. 2013). In addition, an age-related developmental rebound of MD in orbitofrontal limbic areas has been reported in a cohort of marmosets (Uematsu et al. 2017). One possible mechanism to explain these diffusion changes in rhesus monkeys is related to the complex local microstructural texture, cell packing density, or a degree of directional coherence in WM (Schmithorst et al. 2002). A higher degree of fiber tract organization leads to an increase in FA, but not in MD (Takahashi et al. 2000). Therefore, regional FA changes are not always inversely related to MD changes, as shown in Figures S3 and S4. In our analyses, we observed that there were relatively small increases in FA until 20 months of age, with relatively marked increases in MD that occurred around 8 months of age. This pattern of diffusion change may be explained by the evolving structural organization of fiber tracts during development and generation of unmyelinated axons, which occupy less space and enhance water molecule diffusion during late infancy. However, regression analysis results in the generalized additive mixed model should be carefully interpreted (see Tables S2 and S3). At the whole brain level, WM volume and FA demonstrated higher R^2 values than other measures (GM, CSF, and MD). In particular, negative R^2 values were observed in the rebounding curves of MD, which means a horizontal line explains the data better than the fitted model. At the ROI level, GM, WM, CSF, and FA showed higher correlations (R^2 values) with age terms, while MD was associated with lower or negative R^2 values. Therefore, the fitted curves for MD changes with age are relatively less reliable in most regions of the brain due to large within-subject variability.

There are several limitations of this study. One potential limitation is that NHPs were anesthetized multiple time periods to acquire the MRI data, which could have a significant effect on their during critical neurodevelopmental brain development due to neurotoxic effects of anesthesia (Reddy 2012; Andropoulos 2018). Environmental factors such as visual stimulation and housing conditions during infancy period could

modulate the development of cortical changes later in life (Distler et al. 1996). For regional volume measures, we have only one source atlas that was derived from the study population itself, and, therefore, we chose direct label propagation. However, it is known that the quality of label map propagation may be greatly improved when using multiple source atlases (Rohlfing et al. 2004; Klein et al. 2009), a process commonly referred to as multiatlas segmentation and label fusion. Robust tissue segmentation of the monkey brain is still challenging due to low signal-to-noise ratio around subcortical regions and strong bias artifacts around the olfactory cortex and occipital lobes, which require manual segmentation. In this study, we manually corrected the internal and external capsules of WM based on FA images after applying the multivariate algorithm-based T_1w and T_2w images and segmenting them into tissue types using prior data derived from SST. Nonetheless, segmentation of small fiber tracts around the occipital and temporal auditory regions was less accurate, which could lead to underestimation of WM volume. Field maps to correct the geometric distortion of DWI were not available from the dataset; thus, registration errors could have occurred during ROI-wise FA and MD analysis. In addition, even though all monkeys were oriented identically within a stereotaxic platform, geometric distortion mainly affected prefrontal and occipital regions, the impact of which on the younger brains may be worse than the older ones. Temporal regions demonstrated a low signal-to-noise ratio, resulting in underestimation of FA. It is important to consider these limitations when interpreting the projected trajectories and the noise in these data.

In conclusion, dynamic brain developmental patterns were observed in rhesus monkey brains. Understanding these dynamic developmental brain changes is important, as simple comparisons of ICV or DTI metrics between treatment and control groups in developmental NHP models might lead to misinterpretation if characteristic growth trajectories during late infancy or puberty are not carefully considered in study design. Future studies incorporating longer-term follow-up images could elucidate more details of the structural dynamics of brain development in NHPs, as well as humans.

Supplementary Material

Supplementary material is available at *Cerebral Cortex* online.

Funding

Alzheimer's Association Research Fellowship (grant AARF-16-441283 to J.K.); National Institutes of Health (R01 NS091602 to C.T.W., R01 MH116675 to C.T.W., R01 DA038588 to M.M.S., R01 HD090925 to J.H.B. and M.M.S., P50 MH100029 to J.H.B., R01 DA017763 to M.A.N., P50 DA006634 to M.A.N.).

Notes

Conflicts of Interest: The authors declare no conflict of interest.

References

Andropoulos DB. 2018. Effect of anesthesia on the developing brain: infant and fetus. *Fetal Diagn Ther*. 43:1–11.

Avants B, Gee JC. 2004. Geodesic estimation for large deformation anatomical shape averaging and interpolation. *NeuroImage*. 23(Suppl 1):S139–S150.

Avants BB, Tustison NJ, Wu J, Cook PA, Gee JC. 2011. An open source multivariate framework for n-tissue segmentation with evaluation on public data. *Neuroinformatics*. 9:381–400.

Bauman MD, Iosif AM, Ashwood P, Braunschweig D, Lee A, Schumann CM, Van de Water J, Amaral DG. 2013. Maternal antibodies from mothers of children with autism alter brain growth and social behavior development in the rhesus monkey. *Transl Psychiatry*. 3:e278.

Benjamini Y, Hochberg Y. 1995. Controlling the false discovery rate—a practical and powerful approach to multiple testing. *J Roy Stat Soc B Stat Meth*. 57:289–300.

Braunschweig D, Van de Water J. 2012. Maternal autoantibodies in autism. *Arch Neurol*. 69:693–699.

Czervionke LF, Czervionke JM, Daniels DL, Haughton VM. 1988. Characteristic features of MR truncation artifacts. *AJR Am J Roentgenol*. 151:1219–1228.

Distler C, Bachevalier J, Kennedy C, Mishkin M, Ungerleider LG. 1996. Functional development of the corticocortical pathway for motion analysis in the macaque monkey: a 14C-2-deoxyglucose study. *Cereb Cortex*. 6:184–195.

Gennatas ED, Avants BB, Wolf DH, Satterthwaite TD, Ruparel K, Ciric R, Hakonarson H, Gur RE, Gur RC. 2017. Age-related effects and sex differences in gray matter density, volume, mass, and cortical thickness from childhood to young adulthood. *J Neurosci*. 37:5065–5073.

Gilmore JH, Shi F, Woolson SL, Knickmeyer RC, Short SJ, Lin W, Zhu H, Hamer RM, Styner M, Shen D. 2012. Longitudinal development of cortical and subcortical gray matter from birth to 2 years. *Cereb Cortex*. 22:2478–2485.

Hedman AM, van Haren NE, Schnack HG, Kahn RS, Hulshoff Pol HE. 2012. Human brain changes across the life span: a review of 56 longitudinal magnetic resonance imaging studies. *Hum Brain Mapp* 33:1987–2002.

Kim JC, Wang L, Shen D, Lin W. 2016. Biomechanical analysis of normal brain development during the first year of life using finite strain theory. *Sci Rep*. 6:37666.

Klein A, Andersson J, Ardekani BA, Ashburner J, Avants B, Chiang MC, Christensen GE, Collins DL, Gee J, Hellier P *et al*. 2009. Evaluation of 14 nonlinear deformation algorithms applied to human brain MRI registration. *NeuroImage*. 46:786–802.

Knickmeyer RC, Styner M, Short SJ, Lubach GR, Kang C, Hamer R, Coe CL, Gilmore JH. 2010. Maturational trajectories of cortical brain development through the pubertal transition: unique species and sex differences in the monkey revealed through structural magnetic resonance imaging. *Cereb Cortex*. 20:1053–1063.

Kroenke CD, Rohlfing T, Park B, Sullivan EV, Pfefferbaum A, Grant KA. 2014. Monkeys that voluntarily and chronically drink alcohol damage their brains: a longitudinal MRI study. *Neuropsychopharmacology*. 39:823–830.

LaMantia AS, Rakic P. 1990. Axon overproduction and elimination in the corpus callosum of the developing rhesus monkey. *J Neurosci*. 10:2156–2175.

Lebel C, Beaulieu C. 2011. Longitudinal development of human brain wiring continues from childhood into adulthood. *J Neurosci*. 31:10937–10947.

Lenroot RK, Gogtay N, Greenstein DK, Wells EM, Wallace GL, Clasen LS, Blumenthal JD, Lerch J, Zijdenbos AP, Evans AC *et al*. 2007. Sexual dimorphism of brain developmental

trajectories during childhood and adolescence. *NeuroImage*. 36:1065–1073.

Liu C, Tian X, Liu H, Mo Y, Bai F, Zhao X, Ma Y, Wang J. 2015. Rhesus monkey brain development during late infancy and the effect of phencyclidine: a longitudinal MRI and DTI study. *NeuroImage*. 107:65–75.

Liu Z, Wang Y, Gerig G, Gouttard S, Tao R, Fletcher T, Styner M. 2010. Quality control of diffusion weighted images. *Proc SPIE Int Soc Opt Eng*. 7628. doi: 10.1117/12.844748. PMID: 24353379.

Malkova L, Heuer E, Saunders RC. 2006. Longitudinal magnetic resonance imaging study of rhesus monkey brain development. *Eur J Neurosci*. 24:3204–3212.

Meng Y, Jiang J, Bachevalier J, Zhang X, Chan AW. 2017. Developmental whole brain white matter alterations in transgenic Huntington's disease monkey. *Sci Rep*. 7:379.

Oguz I, Farzinfar M, Matsui J, Budin F, Liu Z, Gerig G, Johnson HJ, Styner M. 2014. DTIPrep: quality control of diffusion-weighted images. *Front Neuroinform*. 8:4.

Olson S, Institute of Medicine (U.S.), Committee on From neurons to neighborhoods: Anniversary Workshop., National Research Council (U.S.). 2012. *From neurons to neighborhoods: an update: workshop summary*. Washington (DC): National Academies Press.

Payne C, Machado CJ, Bliwise NG, Bachevalier J. 2010. Maturation of the hippocampal formation and amygdala in *Macaca mulatta*: a volumetric magnetic resonance imaging study. *Hippocampus*. 20:922–935.

Prastawa M, Gilmore JH, Lin W, Gerig G. 2005. Automatic segmentation of MR images of the developing newborn brain. *Med Image Anal*. 9:457–466.

Reddy SV. 2012. Effect of general anesthetics on the developing brain. *J Anaesthesiol Clin Pharmacol*. 28:6–10.

Rohlfing T, Russakoff DB, Maurer CR Jr. 2004. Performance-based classifier combination in atlas-based image segmentation using expectation-maximization parameter estimation. *IEEE Trans Med Imaging*. 23:983–994.

Schmithorst VJ, Wilke M, Dardzinski BJ, Holland SK. 2002. Correlation of white matter diffusivity and anisotropy with age during childhood and adolescence: a cross-sectional diffusion-tensor MR imaging study. *Radiology*. 222:212–218.

Scott JA, Grayson D, Fletcher E, Lee A, Bauman MD, Schumann CM, Buonocore MH, Amaral DG. 2016. Longitudinal analysis of the developing rhesus monkey brain using magnetic resonance imaging: birth to adulthood. *Brain Struct Funct*. 221:2847–2871.

Shi Y, Short SJ, Knickmeyer RC, Wang J, Coe CL, Niethammer M, Gilmore JH, Zhu H, Styner MA. 2013. Diffusion tensor imaging-based characterization of brain neurodevelopment in primates. *Cereb Cortex*. 23:36–48.

Short SJ, Lubach GR, Karasin AI, Olsen CW, Styner M, Knickmeyer RC, Gilmore JH, Coe CL. 2010. Maternal influenza infection during pregnancy impacts postnatal brain development in the rhesus monkey. *Biol Psychiatry*. 67:965–973.

Styner M, Knickmeyer R, Joshi S, Coe C, Short SJ, Gilmore J. 2007. Automatic brain segmentation in rhesus monkeys. *Proc of SPIE*. 6512:65122L.

Takahashi M, Ono J, Harada K, Maeda M, Hackney DB. 2000. Diffusional anisotropy in cranial nerves with maturation: quantitative evaluation with diffusion MR imaging in rats. *Radiology*. 216:881–885.

Tamnes CK, Herting MM, Goddings AL, Meuwese R, Blakemore SJ, Dahl RE, Guroglu B, Raznahan A, Sowell ER, Crone EA *et al*. 2017. Development of the cerebral cortex across adolescence: a multisample study of inter-related longitudinal changes in cortical volume, surface area, and thickness. *J Neurosci*. 37:3402–3412.

Tristan-Vega A, Garcia-Perez V, Aja-Fernandez S, Westin CF. 2012. Efficient and robust nonlocal means denoising of MR data based on salient features matching. *Comput Methods Prog Biomed*. 105:131–144.

Tustison NJ, Holbrook AJ, Avants BB, Roberts JM, Cook PA, Reagh ZM, Stone JR, Gillen DL, Yassa MA. 2017. *The ANTs longitudinal cortical thickness pipeline. bioRxiv: 170209*.

Uematsu A, Hata J, Komaki Y, Seki F, Yamada C, Okahara N, Kurotaki Y, Sasaki E, Okano H. 2017. Mapping orbitofrontal-limbic maturation in non-human primates: a longitudinal magnetic resonance imaging study. *NeuroImage*. 163:55–67.

Vandeleest JJ, Capitanio JP. 2012. Birth timing and behavioral responsiveness predict individual differences in the mother-infant relationship and infant behavior during weaning and maternal breeding. *Am J Primatol*. 74:734–746.

Weisenfeld NI, Warfield SK. 2009. Automatic segmentation of newborn brain MRI. *NeuroImage*. 47:564–572.

Westlye LT, Walhovd KB, Dale AM, Bjornerud A, Due-Tonnessen P, Engvig A, Grydeland H, Tamnes CK, Ostby Y, Fjell AM. 2010. Life-span changes of the human brain white matter: diffusion tensor imaging (DTI) and volumetry. *Cereb Cortex*. 20:2055–2068.

Young JT, Shi Y, Niethammer M, Grauer M, Coe CL, Lubach GR, Davis B, Budin F, Knickmeyer RC, Alexander AL *et al*. 2017. The UNC-Wisconsin rhesus macaque neurodevelopment database: a structural MRI and DTI database of early postnatal development. *Front Neurosci*. 11:29.